Computational Materials Science 244 (2024) 113253

Contents lists available at ScienceDirect

Computational Materials Science

journal homepage: www.elsevier.com/locate/commatsci

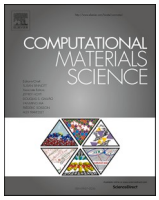

Full Length Article

Examining the mechanics responsible for strain delocalization in metallic glass matrix composites

Casey O. Messick [a], Lin Li [b,*], Eric R. Homer [a,*]

[a] Dept. of Mechanical Engineering, Brigham Young University, Provo, UT, USA
[b] School for Engineering of Matter, Transport and Energy, Arizona State University, Tempe, AZ, USA

ARTICLE INFO

Keywords:
Metallic glass matrix composites
shear transformation zone (STZ) dynamics
Shear band
Dendritic microstructure
Strain delocalization

ABSTRACT

Metallic glass matrix composites (MGMCs) represent a promising avenue for enhancing the ductility of monolithic metallic glass. These composites utilize a secondary crystalline phase to aid in the delocalization of strain. This work seeks to understand the mechanisms underlying strain delocalization in MGMCs to guide further advancements in this class of material. Employing a mesoscale shear transformation zone (STZ) dynamics model, we investigate how variation in dendritic microstructural sizes and spacings impact the shear banding behaviors of MGMCs subjected to uniaxial tensile loading. Statistical analysis of shear banding characteristics reveals that the competition of shear band nucleation and propagation rates can encourage strain delocalization in MGMCs. The introduction of a crystalline dendritic structure into the amorphous matrix increases the number of shear band nucleation events while reducing shear band propagation rates. Furthermore, reducing dendrite sizes leads to greater strain delocalization among more shear bands and delays the onset of run-away shear bands, resulting in lower overall shear band growth rates. Therefore, this study sheds light on the crucial role of dendritic microstructural sizes in influencing shear banding characteristics and strain delocalization in MGMCs, offering valuable insights to inform the design and development of advanced materials with superior mechanical properties.

1. Introduction

Bulk metallic glasses (BMGs) are unique materials that exhibit an impressive combination of high yield strength and high resilience [1,2]. Combined with the ability to undergo conventional glass forming processes, BMGs are promising candidates for small-scale structural applications [3,4]. However, their tendency to localize strain into shear bands has limited their adoption [5–7]. Metallic glass matrix composites (MGMCs) have been developed to overcome this weakness; a secondary crystalline phase in the amorphous matrix leads to strain delocalization and improved toughness [8–10]. Interestingly, monolithic BMGs also exhibit strain delocalization when deformed under high strain rates [11–16]. This paper seeks to determine whether the underlying mechanism governing improved strain delocalization in MGMCs is related to the phenomena leading to more homogeneous behavior in BMGs loaded at high strain rates.

The catastrophic failure of BMGs upon yield is attributed to the rapid growth and development of shear bands. The fundamental unit of deformation underlying this behavior is known as the shear transformation zone (STZ), and is described as a cluster of atoms that undergoes shear distortion to accommodate strain [17]. Although the collective activation of many STZs can vary depending on loading conditions, under normal loading rates and ambient temperatures, multiple STZ activations tend to cluster together eventually forming shear bands [18,19]. Further accumulation of strain, which is typically concentrated in a few shear bands, results in fracture. This entire process is seen to occur over periods of 10^{-5}-10^{-3} s in experiments [20–23].

Research has shown that the shear banding process in BMGs can be disrupted in two ways. In the first way, when monolithic metallic glass is deformed at higher strain rates, a proliferation of shear banding can be seen [13,15,24–26]. This has been demonstrated in nanoindentation [6,27–29]. As metallic glasses are indented at higher rates, serrations corresponding with shear banding decrease in size until they are virtually non-existent [30]. Schuh et al. hypothesized that the change from a few to many shear bands is due to a competition of shear band nucleation and propagation rates. In other words, shear bands enter the nucleation stage at a rate faster than the propagating shear bands can relieve stress, resulting in increased and simultaneous operation of many

* Corresponding authors.
E-mail addresses: lin.li.10@asu.edu (L. Li), eric.homer@byu.edu (E.R. Homer).

https://doi.org/10.1016/j.commatsci.2024.113253
Received 13 April 2024; Received in revised form 17 July 2024; Accepted 19 July 2024
Available online 28 July 2024

shear bands [11,12,16,31].

This hypothesis was corroborated in recent work by Harris et al. [14]. Using STZ dynamics, they were able to numerically simulate the deformation of metallic glass at varying strain rates. Transitions from strong to medium and medium to lightly serrated flow corroborate what is seen from nanoindentation experiments [16]. Accompanying the transition from strongly serrated flow (low strain rates) to lightly serrated flow (high strain rates) was an increase in shear band nucleation rates and a decrease in shear band propagation rates. They were able to verify the hypothesis in [16] that at high strain rates, strain is not accommodated quickly enough to relieve stress resulting in simultaneous shear banding.

The second mechanism for disrupting shear localization involves constrained modes of loading. Conner et al. [32] found that as the thickness of specimens loaded under bending approached the order of shear band length scales, greater bending strains could be observed. Using scanning electron microscopy (SEM), they were able to visualize the growth and development of simultaneous shear banding events. Shear bands propagating from the exterior surface would arrest upon reaching the neutral stress axis, encouraging nucleation elsewhere. Rolled metallic glasses show a similar disruption to catastrophic shear banding, where shear bands from the rolling process disrupt the propagation of new shear bands that could lead to failure [33,34].

As noted previously, the development of MGMCs has yielded substantial improvements in the plasticity of amorphous based alloys [8,35–37]. The extent to which strain is delocalized is influenced by some microstructural characteristics including crystalline volume fraction, size, spacing, and morphology [9,10,36,38–40]. It is well-known that increasing the volume fraction of a ductile crystalline phase results in improved plasticity. This is most effective when a soft crystalline phase is used, but it usually comes at the expense of decreased composite strength [41–48]. Composites with bimodal dendrite sizes also have demonstrated enhanced plasticity as smaller dendrites lead to an increased number of nucleation sites for shear bands, while larger dendrites work more effectively to inhibit their propagation [36,47–53]. Another class of MGMC is known as shape memory MGMCs, where deformation-induced martensitic transformation occurs in the crystalline phase. The thick martensitic plates can broaden the shear bands during propagation. The broad shear bands further induce the formation of more martensitic variants, benefiting strain delocalization [43,54].

In zirconium-based MGMCs by Hofmann et al. [9], which exhibit tensile strain $>$ 10 % and strengths as high as 1.5 GPa, microstructural and fractographic analyses revealed matching length scales between shear band sizes and dendrite spacings. Hofmann et al. hypothesized that dendrites can serve to limit shear band propagation within the domains between the dendrites, thereby arresting crack development. Furthermore, as individual shear bands cannot sufficiently relax strain, the simultaneous operation of multiple shear bands is consequently encouraged [9,55]. However, the physics underpinning this length scale matching remains unresolved.

In the present article, we simulate and examine the shear band characteristics of MGMCs under tensile loading. We focus on quantifying shear band growth and nucleation rates to demonstrate that enhanced plasticity induced by crystalline inclusions actually derives from the inherent competition of rates seen in monolithic metallic glasses deformed at high strain rates or under constrained modes of loading. We simulate the phenomena using the mesoscale STZ dynamics modeling framework. Dendrite length scales are systematically varied to investigate their effects on shear banding characteristics and macroscopic observables. The discussion examines the competition of rates between shear band nucleation and propagation in MGMCs and examines correlations between microstructural dendrite length scales and observed shear banding characteristics.

2. Methodology

2.1. STZ dynamics modeling

In this work, the STZ dynamics model is utilized to simulate the deformation of MGMCs [7]. The STZ dynamics model is a mesoscale simulation technique whose fundamental unit of deformation is the STZ. STZs are modeled as coarse-grained Eshelby inclusions that undergo a transformation strain when selected for activation. Potential STZs are distributed throughout a finite-element mesh such that any region can deform through the activation of an STZ. The rate law governing the activation of STZs is given by:

$$\dot{s} = \nu_0 \bullet exp\left(-\frac{\Delta F - \frac{1}{2}\tau \bullet \gamma_0 \bullet \Omega_0}{kT} \right), \tag{1}$$

where $\dot{s}$ is the STZ activation rate, ΔF is the energy barrier for an STZ activation, τ and T are the local shear stress and temperature in MPa and Kelvin respectively, k is the Boltzmann's constant, γ_0 is the incremental shear strain applied to an STZ, Ω_0 is the volume of an STZ, and ν_0 is the attempt frequency.

The STZ dynamics framework is governed by the kinetic Monte Carlo (kMC) algorithm [56]. While this framework is described in more detail in [7], we provide a brief description here. In each iteration of the kMC algorithm, the activation rate is calculated for all potential STZs. The distribution of these rates is used to determine the elapsed time of that particular simulation step and to select the next STZ for activation, where the selection takes into account the relative probability of the various potential events (e.g. low and high activation rate events have a low and high probability of being selected, respectively). The finite element solver assigns eigenstrains to elements corresponding to the STZ event selected for activation and then determines the new stress state, after which the process is repeated until the simulation is terminated.

Whereas normal rejection-free kMC allows all events to occur, we employ a modification to ensure that any given step doesn't move time forward by too large of an increment, and thereby allow the system to account for the changes in the external boundary conditions [56]. For this work, we employ a maximum time step of 1 s. This maximum time step is then used to suppress any STZ activations that would require a time step larger than 1 s. When this happens, rather than activate an STZ, the system steps forward by 1 s and resultant stresses and strains are updated throughout the mesh. The system then reevaluates the STZ activation rates and allows another STZ activation to be attempted. For a simulation 300 nm in height and a strain rate of 10^{-3} s^{-1}, this leads to a maximum possible displacement of 0.3 nm per step.

Since we desire to model MGMCs, we employ a deformation model for a secondary crystalline phase, that was added to the STZ dynamics framework by Hardin et al. [57]. In this approach, the finite element mesh is partitioned into two phases and each partition follows its own material model; STZ activations for the amorphous regions, as described above, and metal plasticity for the crystalline regions, as described below. The application of each material model to its respective phase is consistent with other modeling approaches [58–62]. The boundary condition between the two phases consists of coincident nodes that act as a perfectly bound no-slip condition between the two phases. This no-slip condition is consistent with several modeling approaches [58–60], though at least one approach has been chosen to apply frictional contact between the two phases [61]. It is not clear which approach is best in MGMCs where the bond between phases is strong.

The crystalline model follows a ductile plastic constitutive law based on a Taylor dislocation model and the work of Qiao et al. [63] and Zhang et al. [51]. The tensile stress–strain relationship of this model is given by the following:

$$\sigma = \sigma_{ref}\sqrt{\left(\frac{\sigma_y}{E} + \varepsilon^p\right)^{(2n)} + L\bar{\eta}}, \quad (2)$$

where ε^p is the plastic strain, E is Young's modulus, and σ_y is the yield stress. $\sigma_{ref} = \frac{E^n}{\sigma_y^{n-1}}$, where n is the hardening coefficient. $L = 180b\left(\frac{a\mu}{\sigma_{ref}}\right)^2$ is defined as the intrinsic material length where μ, b, and a are the shear modulus, Burgers vector length, and an empirical constant of 0.1 respectively. $\bar{\eta}$ is the average strain gradient approximated by $\frac{\varepsilon^p}{D}$ where D is a characteristic diameter of the crystalline phase microstructure.

Stress or deformation loading is applied in accordance with standard finite element methods. By combining these two material models, one can vary the morphology of the microstructure of the secondary phase and examine its effect on the shear banding process.

2.2. Model implementation

To examine the mechanical behavior of the simulated MGMCs, 2D simulation cells are subjected to uniaxial tension at a constant strain rate of 10^{-3} s^{-1} (or 0.3 nm/s) along the longest dimension of the simulation cells, which are 300 nm tall and 100 nm wide. These dimensions are limited by computational constraints; though these dimensions are smaller than those typically seen in studies of MGMCs, the observed trends do support those seen at larger length scales. The modeling framework has not incorporated a failure mechanism so each simulation terminates when it reaches 0.035 strain, which provides sufficient strain to characterize shear banding in the specimen.

The parameters for the amorphous and crystalline phase material models are listed in Table 1. The parameters of the amorphous phase have an STZ volume of 2.2 nm^3 and an activation energy barrier of 1.59 eV [64], which lead to an approximate yield strength of 2.1 GPa; these values are derived from the STZ dynamics work by Harris et al. [14], capturing the stress–strain behavior of Vitreloy 1. The mechanical properties of the crystalline phase require both yield strength and strain hardening exponent, as indicated in **Eq. (2)**. For this work, we employ a yield strength of 900 MPa and a strain hardening exponent of 0.3. These values were determined from a combined simulated-experimental nanoindentation work and match reported values for crystalline alloys with complex compositions [65–69] (see appendix for more information). A characteristic stress–strain curve for the crystalline and amorphous phases is provided in Fig. 1.

2.3. Modeling dendritic structures in MGMCs

Hardin et al. [57] modeled MGMCs with circular inclusions, which while consistent in morphology and length scale for some composites [70–73] are not necessarily representative of many MGMCs created through a variety of alloy compositions and processing techniques [9,35,38,40,42,55,73–81]. Despite being a mesoscale modeling framework, STZ dynamics is not yet capable of simulating the micron-sized length scales of dendritic microstructures observed in many experiments. To this end, 2D SEM images of DH3 composites [9] are used to create the microstructure for the current work, but at smaller length scales than the reference microstructures. While it is again noted that these dendrite-length scales are smaller than seen in some studies [82–85], these dendrite sizes are of the same order of magnitude as those employed in atomistic studies [70] and larger than nanocrystalline inclusions experimentally observed in certain alloys [71,72].

Table 1
Model parameters for amorphous and crystalline phases.

Property	Symbol & value
Amorphous parameters	
Shear modulus	$\mu = 35.69$ GPa
Poisson's ratio	$\nu = 0.352$
Debye temperature	327 K
Activation energy barrier	ΔF=1.59 eV
STZ shear strain	$\gamma_0 = 0.1$
STZ volume	$\Omega_0 = 2.2$ nm^3
Crystalline parameters	
Shear modulus	$\mu = 39.96$ GPa
Poisson's ratio	$\nu = 0.33$
Yield stress	$\sigma_y = 900$ MPa
Microstructure length	D=50 nm
Burger's Vector	$b = 2.858$ Å
Empirical constant	$a = 0.1$
Hardening coefficient	$n = 0.3$

To systematically vary the dendrite length scales, a target or desired dendrite length scale for each simulation is selected and the digitized microstructures from the SEM images are scaled to achieve that target dendrite size. The image is converted into a binary matrix and mapped onto the finite element mesh, partitioning the Finite Element Analysis (FEA) model into two phases. In the research literature, the dendrite size (L) and dendrite spacing (S) have been commonly utilized, where L is the total spanning length of a single dendrite tree and S is the average distance between the center of one dendrite tree to another approximated as the diameter calculated from the dendrite area [41,50,86–88]. However, to better capture the effects of dendrite and amorphous sizes, we will instead be reporting average dendrite (L_D) and amorphous (S_D) domain sizes where L_D is the average diameter of a single crystalline domain in 2D and S_D is approximated as the distance spanning across amorphous domains from dendrite edge to dendrite edge (calculated by subtracting the average crystalline domain sizes from the average dendrite domain to adjacent dendrite domain center-to-center distances). See Fig. 2 for examples of L_D and S_D. Upon transposing 2D images of dendritic structures onto the finite element mesh, some discrepancy does exist between the binary matrix and triangular mesh, but by using a dense mesh (about 103,000 elements), the effects are minimized (see Fig. 2). Consistent with previous research, [41,50,86,87,88], we do not consider variability in these metrics due to microstructural fluctuations; this opportunity is left for future work. The consistency in the scaled microstructures means that the average dendrite size (L_D) is sufficient to account for what is changing between the different simulations.

2.4. Microstructure sampling methodology

In this work, we examine the effect of different microstructural length scales that all have the same overall volume fraction of the crystalline phase. We examine 4 different dendrite length scales, and for each we test 3 different simulation cell morphologies. Due to the stochastic nature of the modeling framework, identical models run multiple times will yield different responses. As such, each morphology is run twice resulting in a total of 24 simulations. The microstructural variables for the different simulations are listed in Table 2. Analysis will focus on dendrite domain sizes (L_D), since amorphous domain sizes (S_D) scale with dendrite domain sizes when volume fraction is held constant. Example morphology from each level is shown in Fig. 3.

2.5. Shear band analysis approach

After each simulation is run, shear banding characteristics are calculated and analyzed. The plastic strains corresponding to each element in the finite element mesh is calculated every 5 steps. The equivalent plastic strains in elements of the amorphous phase come from STZ activations while the strains in elements of the crystalline phase come from the Taylor dislocation model. Therefore, for shear banding characterization, any amorphous elements that accumulate plastic strain are counted as part of the shear banding network. However, for the crystalline phase, by the end of the simulation, every element has accumulated some degree of plastic strain. In order to analyze which elements are part of the shear banding network, a strain threshold is implemented. Crystalline elements that do not meet this threshold are

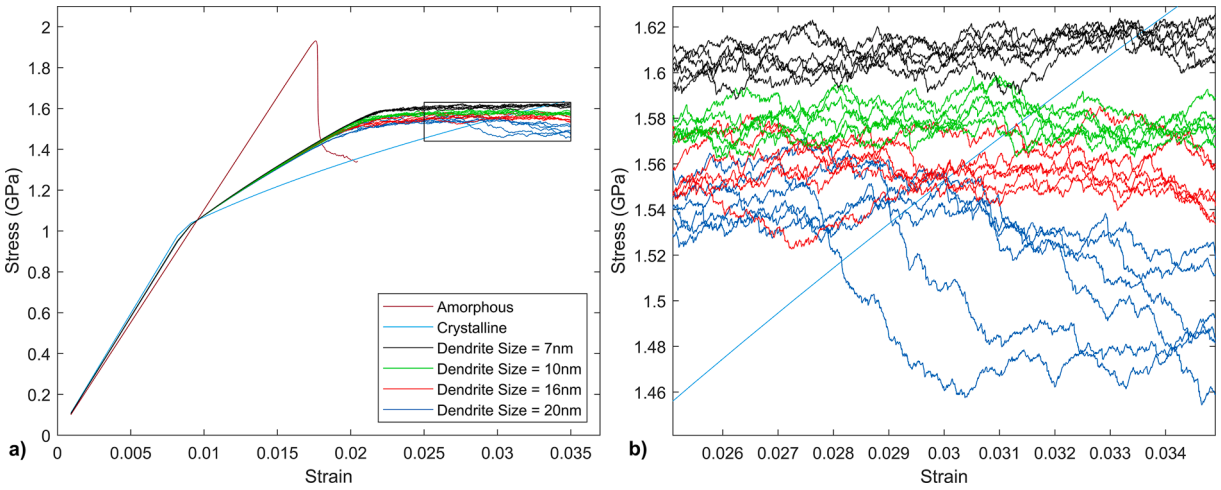

Fig. 1. a) Stress–strain curves for all the simulations (see Sections 3 and 4 for results and discussion). Included are characteristic stress–strain curves for the amorphous and crystalline phases using the material properties in Table 1. b) is a zoomed-in plot of the black rectangular box seen in a).

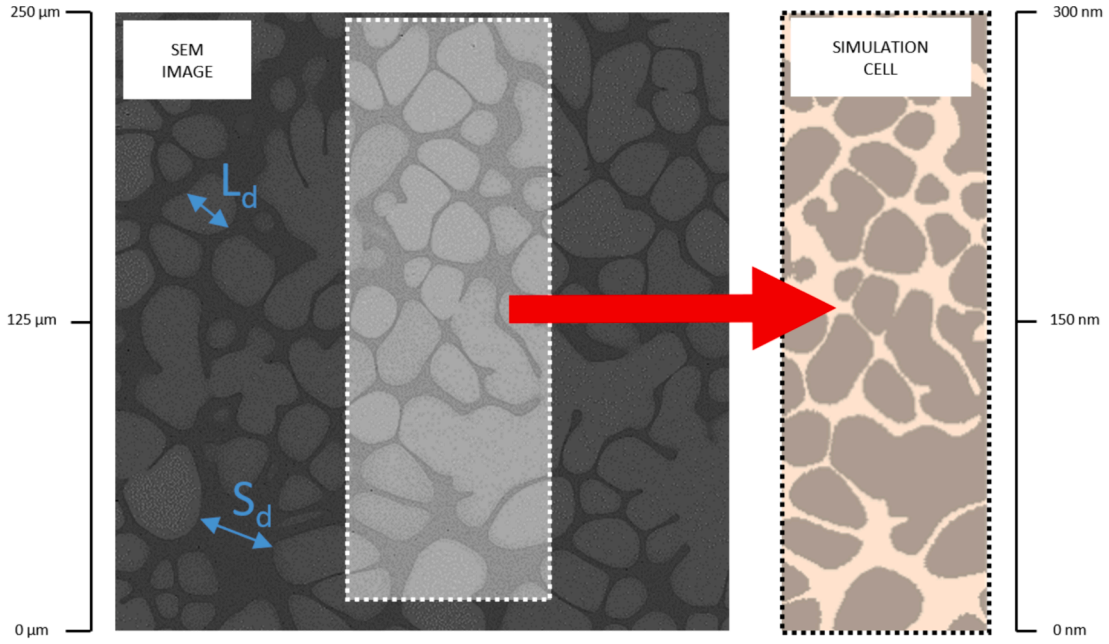

Fig. 2. Using SEM images to systematically mimic and vary dendritic microstructure. Examples of L_D and S_D are illustrated on the SEM image on the left.

Table 2
Systematic variation of dendrite microstructural features.

Simulation	L_d (nm)	S_d (nm)	Volume Fraction
1	7	17	64.6 %
2	10	23	64.8 %
3	16	38	64.8 %
4	20	50	64.3 %

not counted as part of the shear banding process. Although the exact value is subjective, varying levels were examined and a strain value of 0.03 provides a good approach for analysis of the shear banding growth.

For grouping of elements into shear bands, finite elements in either phase that meet the aforementioned criteria and are connected by at least one node are considered to belong to a single shear band. After grouping elements into individual shear bands, the shear band areas are calculated and only those shear bands that meet a minimum shear band size are included in the shear band characterization analysis. The goal with this size threshold is to reduce the likelihood of mistakenly counting one shear band as multiple smaller nuclei that are not yet joined by a node while at the same time still distinguishing the emergence of multiple distinct shear bands that eventually join together. The threshold also helps eliminate misleading propagation rates when shear band nuclei still consist of just a few STZs. For example, the addition of one STZ to another lone STZ would result in a 200 % growth rate.

As is the case with any nucleation type growth, size thresholds are somewhat subject to interpretation. Li et al [89] report a critical nucleation size of 10–20 nm in diameter by simulating a mode I fracture using molecular dynamics. Harris et al. [14] report critical nucleation sizes anywhere from 15-30 nm^3 using STZ dynamics when strained at 10^{-3} s^{-1}. A brief study by varying different nucleation sizes (15–29 nm^2) and analyzing the resulting shear band nucleation rates yielded little variation. As such, a threshold of 15 nm^2 is chosen (or a cluster of roughly 5–7 STZs).

Once shear bands reach the threshold size, each new shear band and all its elements are classified and assigned a shear band identity. As the

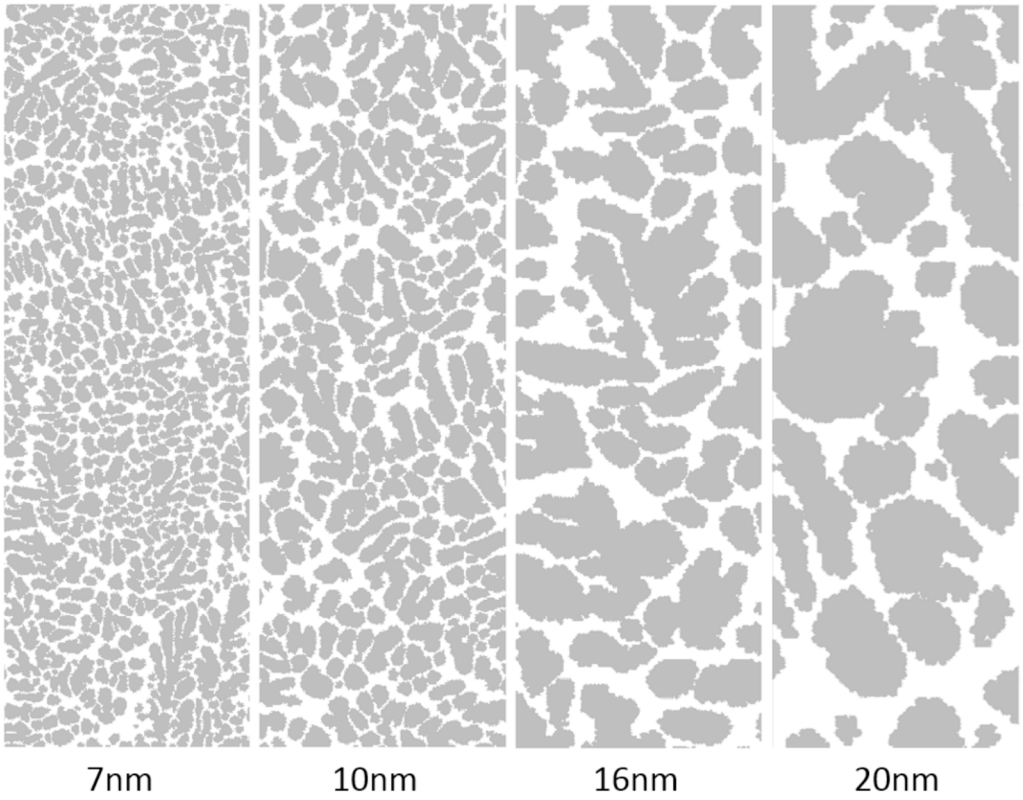

Fig. 3. Example morphology at each dendrite size labeled below each image.

simulation progresses, shear band identities are maintained unless multiple shear bands merge into a single shear band. When this occurs, the identity of the largest shear band is maintained and all elements belonging to the now singular shear band follow this identity. After elements have been assigned to shear bands and evolution tracking of shear bands has been stored, it is somewhat straightforward to then measure the following shear banding characteristics.

2.5.1. Localization index (Γ)

The localization index, Γ, provides a macroscopic measure to help classify the distribution of plasticity throughout the specimen and is introduced in [90]. It is calculated at the end of the simulation using the following:

$$\Gamma = 1 - \frac{\left(\sum_n \gamma_n^2\right)^2}{N\sum_n \gamma_n^4} \tag{3}$$

where γ_n is the plastic strain associated with each of the N elements of the sample. Γ ranges from 0 to 1 where 0 represents a uniform strain distribution and 1 represents strain being concentrated in an infinitely small region. Homer et al. report that values less than 0.5 correspond to homogeneous flow, with a superimposed background of noise, as expected in a disordered solid. In practice, this measurement doesn't typically have a large spread since there is some degree of localization in each simulation, but there is still insight that can be gained despite the small numerical differences.

2.5.2. Nucleation rate (#SBs)

The number of shear bands can easily be counted and provides one measure of nucleation rate. The number of shear bands can be counted in two ways: 1) the number of shear bands that nucleate throughout the simulation and 2) the number of shear bands that exist at the end of the simulation. These numbers differ because many shear bands that nucleate will eventually merge with another shear band. Therefore, the number of shear bands that nucleate throughout the simulation is expected to be significantly higher than the number of shear bands at the end. In either method, the number of shear bands is divided by time to provide a nucleation rate.

2.5.3. Propagation rates ($\dot{\epsilon}_{SB}$)

There are numerous ways to calculate the overall growth rate of shear bands. In this work, the measure of propagation rate is obtained by calculating the rate of change of the area-averaged strain towards the end of the simulation for the largest shear band. This is done by calculating a linear fit of the area-averaged strain vs. time and taking the slope of that line. Shear bands that grow from joining together with another shear band are ignored. Towards the end of the simulation, strain rates of dominant shear bands are relatively constant which provides a more consistent propagation rate value. In this work, of the total 3.5 % strain, at which the simulation is terminated, only the last 0.3 % strain is used to calculate this measure as strain growth rates are relatively constant after this point. While only the rate of strain accumulation in the largest shear band is calculated (also identified as the run-away shear band), using the largest shear band or a few of the largest shear bands yields little variation. A negative rate can be calculated if additional strain elements that join the shear band have a strain lower than the average strain in the shear band in the step prior. This does not necessarily mean that the shear band is no longer growing but that the rate at which it is growing has decreased. This measure will provide insight as to how shear band growth is affected by microstructural sizes.

2.5.4. Involvement of the crystalline phase (C)

The crystalline phase's degree of involvement in the overall shear banding process is reported as the overall percentage of shear band elements that are crystalline. This will be used to shed further light on the competition of shear band nucleation and propagation rates.

2.5.5. Proportion of strain localized in 3 largest shear bands (L_1)

The fraction of strain that is accumulated by the 3 largest shear bands at the end of the simulation is measured. This will describe the degree of localization in a specimen and how shear banding participates in strain accumulation. Measuring the strain localized in too few shear bands (1 or 2) can lead to artifacts in the results where a simulation seems to show little localization when it is highly localized across a small number of shear bands. Conversely, if strain localization is measured across too many shear bands, the results would be difficult to differentiate and would simply show the accumulation of strain by the entire simulation cell. It was chosen that strain would be measured in the 3 largest shear bands as it correlated well with localization indexes as well as the strain maps.

2.5.6. Shear band domination (D)

During the early stages of shear banding in MGMCs, numerous shear bands may compete before a run-away shear band occurs. During this competition, shear bands may alternate between which shear band is propagating the fastest for periods of time. The number of shear bands that take their turn dominating a simulation is calculated and reported. This will be used to understand how quickly strain is localized in a shear band.

3. Results

Fig. 4 shows examples of simulations run at each microstructural size, representing the results of 4 of the 24 simulations in this work. The images are taken at the end of each simulation (0.35 strain). The dendrites are shaded in gray while the white areas denote amorphous regions; these dendritic structures are identical to those shown in Fig. 3. The blue and red fields are the plastic strains experienced by the crystalline and amorphous phases respectively.

We begin by making a few observations about the deformation observed in Fig. 4. First, it is quite easy to see that the degree to which the crystalline phase participates in shear banding is much higher in the smaller dendrite composites. The composites with larger dendrites tend to only propagate through a dendrite when it traverses narrow or short sections of the dendrite. Shear bands that encounter the full thickness of a large dendrite seem to often be obstructed and kept from propagating further into and through the dendrite. The second observation focuses on the more obvious shear localization in the larger dendrite simulations. Subsequent sections focus on a quantitative analysis of the results for all 24 simulations over the 4 microstructural length scales.

Stress–strain curves for all simulations are shown in Fig. 1. Upon yielding of both phases at $\sim$ 2 % of strain, steady state plastic flow is achieved. The flow stress values are higher for the smaller dendrite sizes. The existence of the crystalline phase mitigates the strain-softening behaviors of the amorphous phase, thus maintaining the flow stress at a high level. Such improvement in the mechanical responses can be attributed to shear banding mechanisms and micro-stress state in the dual-phase samples, which will be discussed later. However, it is noteworthy that this response can be impacted by the two key assumptions in the model: 1) strain hardening in the crystalline phase, and 2) the absence of failure mechanisms. Without further experimental validation of dendritic microstructures at these length scales, it is difficult to know how much impact these assumptions have, making these possible areas of improvement for future STZ dynamics models.

Shear band characteristics for each simulation were calculated as described in section 2.5. Box plots of each of these characteristics are shown in Fig. 5 as a function of dendrite size. As can be seen, the various shear band characteristics are consistently influenced by the dendrite size. In Fig. 5a, the localization index, Γ, increases at larger dendrite sizes (though its relatively high magnitude ($\Gamma > 0.8$) indicates that all simulations exhibit localization to some degree). This corresponds well with the results shown in Fig. 5e, where the proportion of strain localized in the 3 largest shear bands also increases at larger dendrite sizes. It is further corroborated by the results in Fig. 5f, where the number of dominant shear bands decreases as dendrite sizes increase, again demonstrating greater localization of strain among fewer shear bands. In Fig. 5d it can be seen that the amount of the crystalline phase that

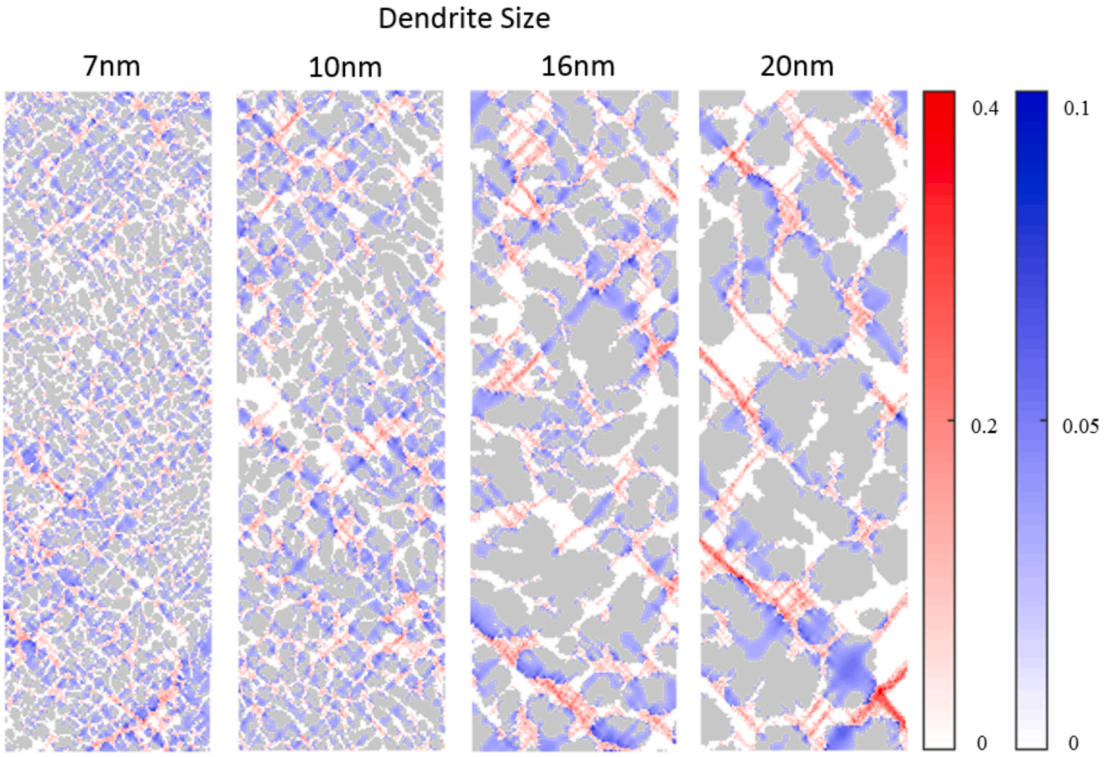

Fig. 4. An example of each microstructural size evaluated. The blue and red fields delineate the plastic strain in the crystalline and amorphous phases respectively (shaded gray areas are crystalline and white areas are amorphous).

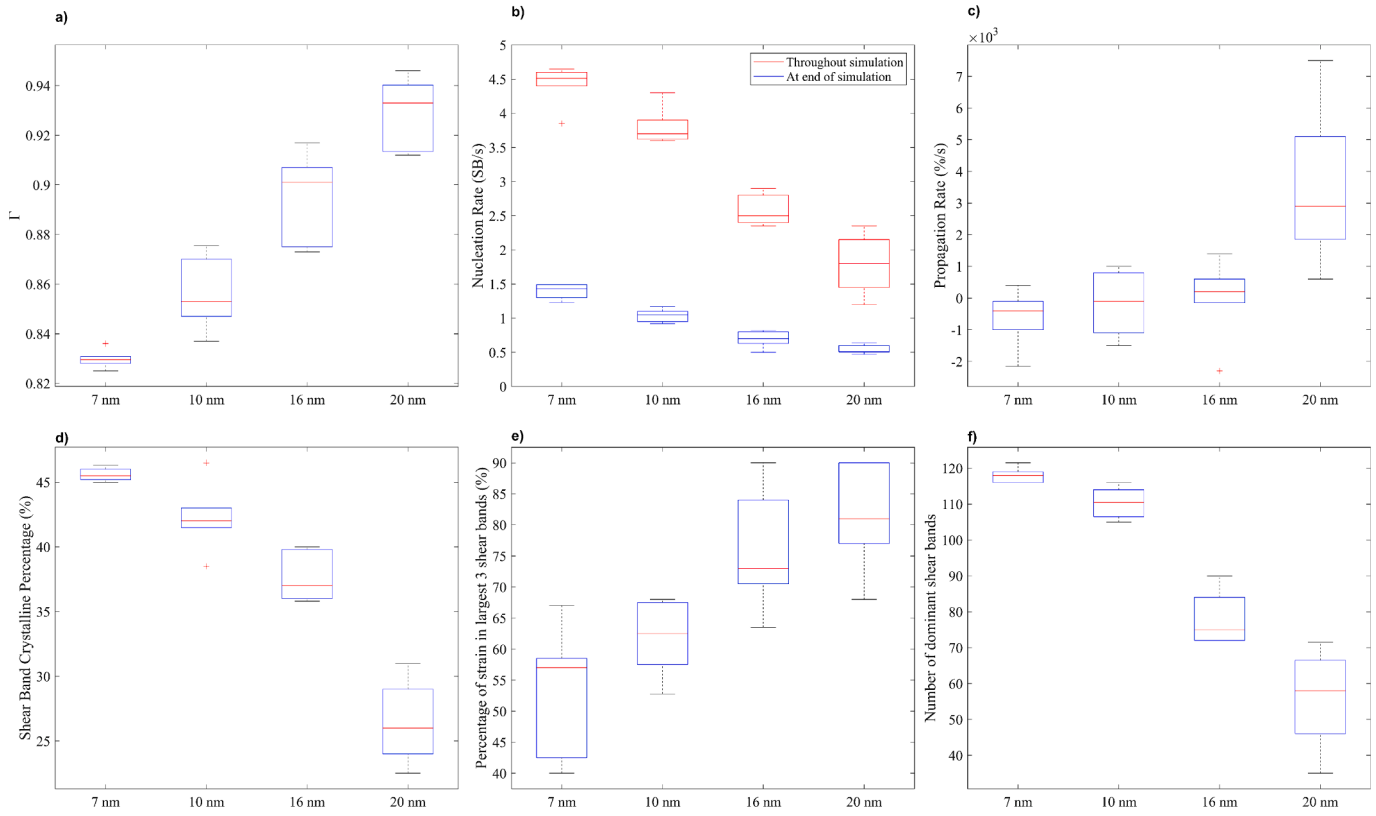

Fig. 5. Box plots of macroscopic measures of strain localization: a) Localization Index b) Number of shear bands c) Propagation rates d) Involvement of the Crystalline phase e) Proportion of strain localization in largest shear bands f) Shear band domination.

contributes to shear banding drops from more than 45 % to under 30 % as the dendrite size changes from the smallest to the largest length scales. Fig. 5b and Fig. 5c correspond well together demonstrating a competition of rates. In Fig. 5b, as dendrite sizes increase, the nucleation rate decreases. Whereas, in Fig. 5c, as dendrite sizes increase, the propagation rate increases. The propagation rate increases from as low as $-0.04\ \%\ s^{-1}$ to as high as $0.29\ \%\ s^{-1}$. At the smaller dendrite sizes, the largest shear band has little to no strain accumulation. All of these observations together suggest a transition resulting from the nucleation and propagation rates.

4. Discussion

4.1. Competition of rates

As mentioned previously, the competition of shear band nucleation and propagation rates are of interest in this work. This competition of rates has previously been demonstrated in purely amorphous metals strained at high rates [14,16]. This work demonstrates that the same phenomena exists in MGMCs and sheds light on the underlying mechanisms behind strain delocalization. These simulations enable a detailed view of the characteristics of shear banding in MGMCs. Further, the stochastic nature of the simulations allows some variability in results, which better simulates a real-world examination of the effect of an averaged microstructural quantity.

Nucleation and propagation rates are superimposed onto the same figure using normalization by their respective largest calculated values shown in Fig. 6. This figure demonstrates the competition of rates previously seen in metallic glasses at high strain rates. The relationship between dendrite size and these shear band characteristics demonstrates strong support for the hypothesis that an introduction of the crystalline phase results in strain relief via two mechanisms: 1) by lowering the propagation rates of shear bands and 2) by increasing the nucleation

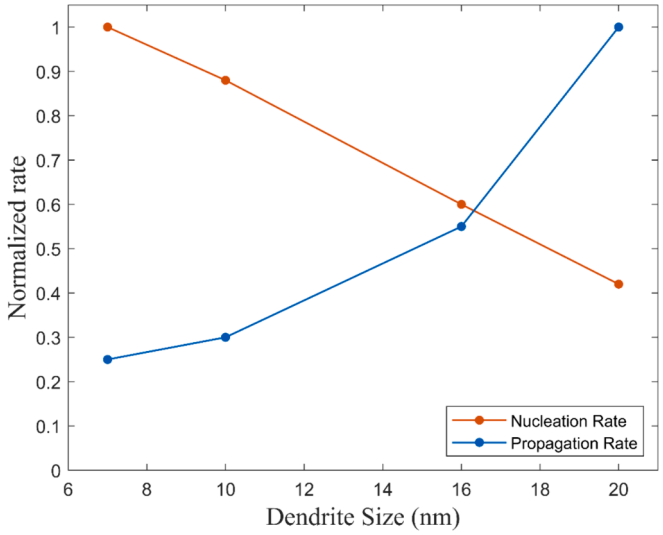

Fig. 6. Competition of rates. Comparison of mean values of measured nucleation (blue) and propagation rates (orange). The relationship of dendrite sizes with nucleation and propagation rates supports the hypothesis that increased homogeneous flow is a direct result of strain relief by competition of rates.

rates of new shear bands. The net effect is that the dendritic phase works to limit shear band propagation rates and encourage shear band nucleation rates resulting in reduced accumulation of strain in one or a few shear bands as seen in purely amorphous specimens.

For the dendrite sizes examined here, there is clearly a lack of local minima or maxima for shear band nucleation or propagation rates. In other words, there is no optimal microstructural size that works best to

delocalize strain. This contrasts with the reported optimal matching of dendrite length scales and shear band crack initiation sizes [9], though it is noted that the present work is at smaller length scales. For the data shown, the greater homogenization of strain the smaller the dendrites. These trends suggest that attempts at decreasing dendrite size experimentally may result in an increased number of shear bands and strain delocalization.

This work suggests that the mechanism responsible for strain delocalization in MGMCs is the competition of nucleation versus propagation rates that work to limit strain accumulation in one to a few shear bands. As a direct result, this work then also proposes the method for greater strain delocalization in MGMCs is two-fold: 1) encourage shear band nucleation throughout the specimen and 2) decrease the rate of growth of shear bands. The question then remains, what exactly encourages greater shear band nucleation? And consequently what then discourages them from accumulating more strain once nucleated?

4.2. Examination of shear banding in MGMCs

One of the great benefits of using numerical simulations is the ability to examine much smaller time and length scales. This allows us to resolve mechanics not visible to experimentation such as the early stages of shear banding. Of particular interest here is understanding specific conditions that encourage shear band nucleation and propagation.

To better understand the mechanisms behind the competition of rates, we examine the conditions for initiation of STZs, nucleation of shear bands, and growth of shear bands.

4.2.1. Initial STZ activations

Snapshots of stress fields immediately after the first STZ activation in two example simulations at two microstructural sizes are shown in Fig. 7. The coloring denotes stress and the vibrancy of the color conveys the magnitude of stress. Early in the simulation, there is essentially uniform strain in the crystalline dendrites and large areas of stress concentration occur mostly at the dendritic-amorphous interfaces. Red dots signify the location of the first STZ activation in each of these simulations. Due to the nature of the STZ dynamics modeling framework, areas of high stress are, although not guaranteed, much more likely to experience an STZ activation than others. This is verified by the first STZ activations happening in one of the highest stress concentrations on the maps. This is consistent with what has already been noted in literature [91].

When examining the large dendrites in Fig. 7b), stress concentrations are particularly prevalent where there exist dendrites spanning both sides of a glassy domain along a 45° angle to the longitudinal axis or planes of highest resolved shear stress. Stress concentrations are higher the smaller the domain. Therefore, it can reasonably be inferred that in order to disperse STZ activations throughout the specimen, smaller domains will provide a larger number of desirable sites for STZ activations for uniaxial tensile specimens. This could be achieved successfully with many small dendrites.

Conversely, when looking at Fig. 7a), there is an increased number of high-stress sites although the magnitudes are lower. This is verified in Fig. 8, which shows a plot of the maximum local Von Mises stress values in the same specimens over time. This demonstrates that stress values are on average lower when dendrites are small. The inset in this figure also shows that stress concentration levels are higher before the first STZ activation in simulations with large dendrites than in simulations with small dendrites. This means that STZ activations have less reason to cluster and therefore operate collectively in a more homogeneous manner in specimens with smaller dendrites as stress concentrations are lower in magnitude.

4.2.2. Shear band nucleation or STZ clustering

STZ clustering in MGMCs occurs in a different fashion than in pure amorphous metals. In monolithic metallic glass, STZ clustering happens

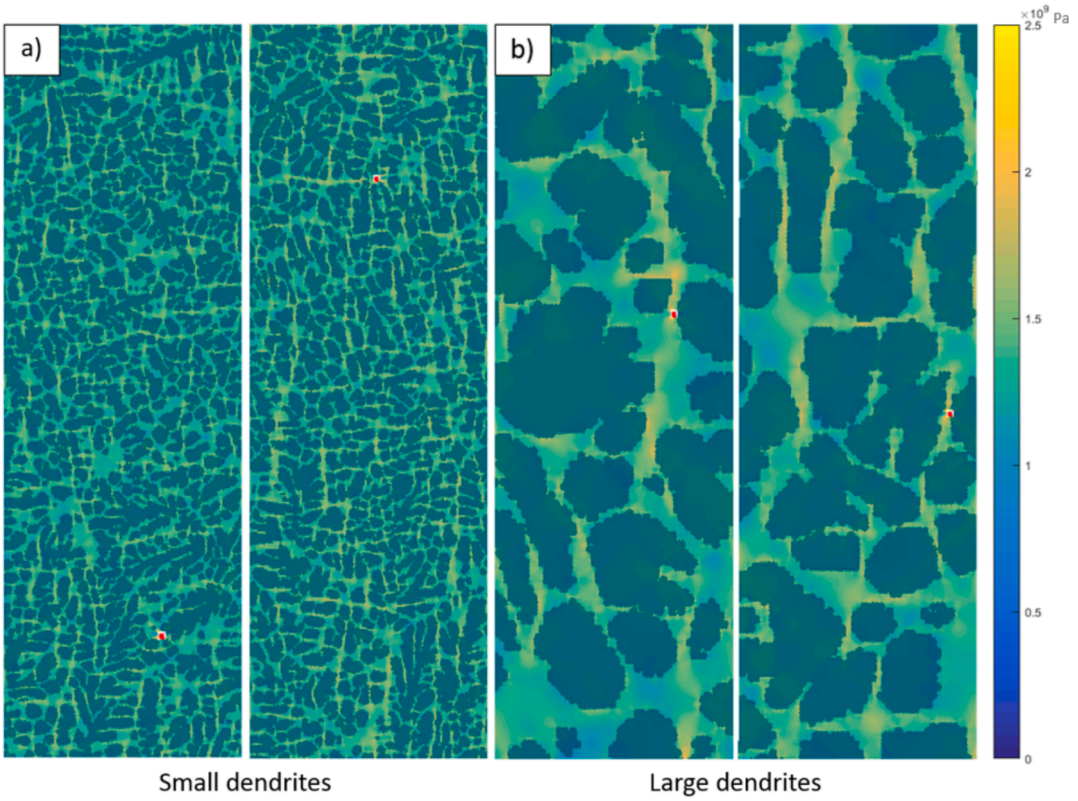

Fig. 7. Examining the stress fields in two example simulations with a) small dendrites ($L_d = 7$ nm) and b) large dendrites ($L_d = 20$ nm) immediately after the first STZ activation occurred (denoted by red dots).

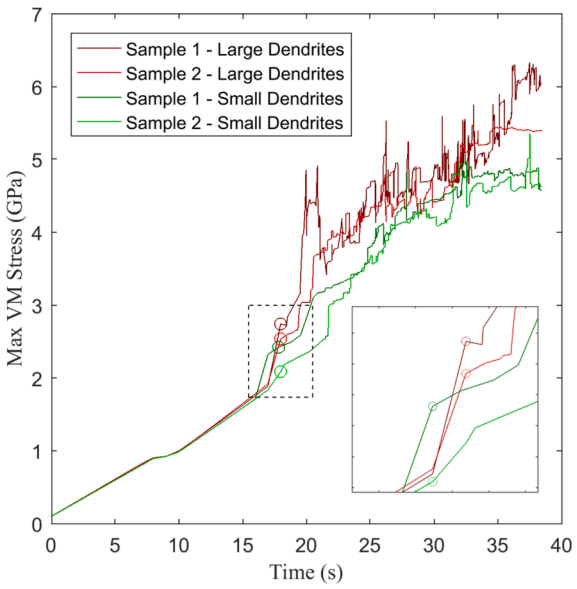

Fig. 8. Comparison of maximum Von Mises (VM) stresses in two large vs. two small dendrite simulations. The inset shows stress concentrations at the time of the first STZ activation in each simulation. Circles denote the first STZ activations in each of these simulations.

much faster and with far fewer clusters [18]. In MGMCs, due to restricted domains and an increased number of stress concentrations from elastic mismatches, STZ clustering is encouraged to occur for an extended period of time. This is demonstrated in Fig. 9, which shows the number of shear bands that exist as the simulation progresses. The shear band nucleation stage exists for as long as the number of shear bands is growing. When the number of shear bands begins to decrease, shear bands are now propagating and absorbing other shear bands and the STZ clustering stage has ended. Where shear band growth is the governing stage in amorphous metals, STZ nucleation appears to be the governing stage in MGMCs.

For the simulations run here, the shear band nucleation stage is longer for MGMCs with smaller dendrites (Fig. 9). When dendrite sizes are decreased, the number of suitable nucleation sites increases. This encourages shear bands to nucleate in more areas. The number of shear bands in the simulations with larger dendrites increase more quickly in the beginning. However, they also peak earlier in the simulation as shear bands begin to run away and absorb other shear bands at lower stress levels.

As the process of STZ clustering is viewed, there seems to be no reason for one region to be more likely to accumulate STZ clusters than any other region in the specimen. After the first few initial STZ activations throughout the specimen, the choice of which STZ will first accumulate more STZs seems to be random, suggesting homogeneous deformation during this early stage. Furthermore, no significant trends were found as to which shear band nuclei will continue to grow in size and which will not.

4.2.3. Shear band propagation

There are numerous ways in which shear bands interact with dendrites [57]. Smaller dendrites are more prone to participate in shear banding as shear bands can propagate through the dendrite. Larger dendrites tend to act as a barrier and shore up strain accumulation at the dendrite-matrix interface. This is shown in Fig. 10, which plots the degree of participation by the crystalline phase in shear banding over time for the same 4 example simulations examined previously. The simulations with smaller dendrites on average saw a larger participation in shear banding by the crystalline phase. This can have three repercussions: 1) ductility is enhanced as the crystalline phase is accommodating more strain, 2) crack initiation is likely delayed or discouraged from happening in the metallic glass phase as there is a less overall strain in the metallic glass matrix, and 3) shear bands propagate slowly through crystalline dendrites resulting in shear bands not being able to relax the specimen sufficiently fast enough which encourages strain accumulation in other shear bands.

On the other hand, simulations with large dendrites will tend to stop a shear band at the interface between the dendrite and glass matrix. Interestingly, this appears to be less desirable than having the shear band propagate through the dendrite. This is because shear bands that grow through a dendrite will dissipate stress concentrations better than shear bands piling up at the interface. Eventually, enough stress will accumulate that will then propagate the shear band very quickly through the dendrite resulting in a run-away shear band. In this sense, smaller dendrites are more desirable as more of the crystalline phase participates in shear banding earlier in the simulation.

4.3. Correlation with experimental work

Although the length scales examined in this work are smaller than

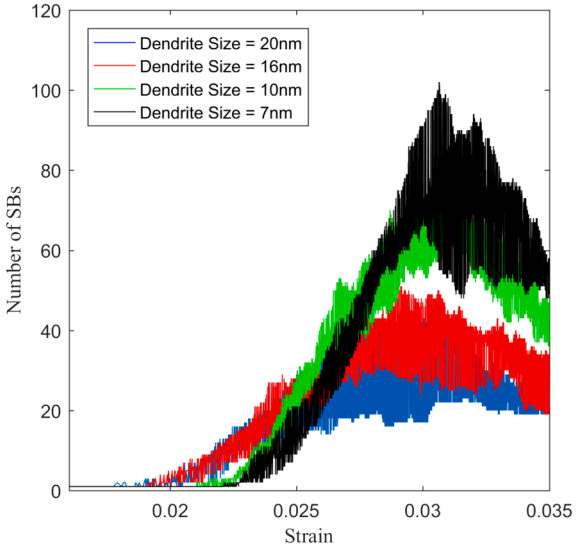

Fig. 9. The number of shear bands during the straining of each simulation. All six simulations for each dendrite size are plotted together as one large data set.

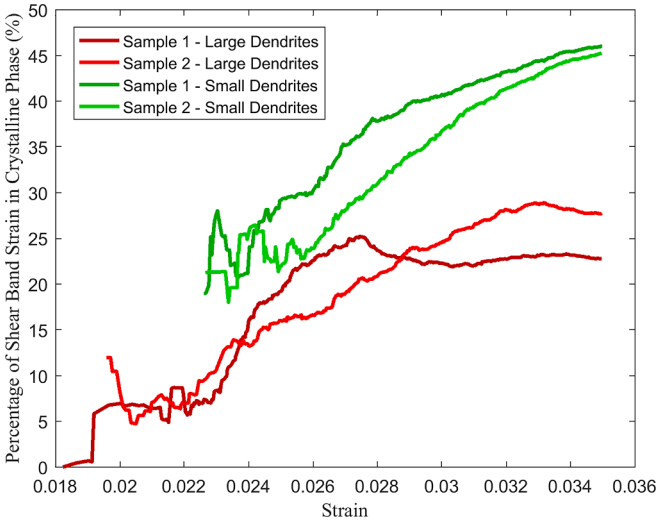

Fig. 10. Percentage of shear band strain carried by the crystalline phase in two large (L_d = 20 nm, green) and two small (L_d = 7 nm, red) simulations.

typically reported in experiments, the trends observed demonstrate a favorable correlation. First, as previously mentioned, it is widely acknowledged that higher volume fractions of the crystalline phase result in significantly increased plasticity. A softer crystalline phase is believed to reduce shear band propagation velocities by lowering stresses when shear bands encounter crystalline regions [41–48]. Although volume fractions were held constant in this study, it is evident that as the degree of participation in strain by the crystalline phase increases, a similar effect is observed, where propagation velocities of shear bands decrease.

Additionally, some groups have found that a bimodal distribution of dendrite sizes can enhance plasticity. The hypothesis posits that smaller dendrites can serve to initiate a greater number of shear bands [53,92]. The greater number of nucleation sites due to small dendrites is corroborated by this work. A clear correlation emerges between reduced dendrite sizes and increased nucleation rates, and this may be attributable to factors such as the nature and size of the interface between phases (see Supplementary Figure S1) [93].

Recently, several crystalline-amorphous dual-phase nanocomposites have been fabricated [94–96], where both the crystalline and amorphous phases have the characteristic length scale on the order of nanometers. By tuning the microstructural features, these materials can achieve superior strength and desirable plasticity characteristics by promoting the formation of multiple shear bands and impeding the propagation of localized shear bands. Our study here offers mechanistic insight into strain delocalization and favorable shear banding behaviors, providing a foundation for the design of nanoscale structural features aimed at enhancing material properties. Further advancements in refining constitutive descriptions of the crystalline phase, along with subsequent studies at such length scales with varying volume fractions and nano-crystallite constitutive law [97,98], hold the potential to solidify and expand upon these findings.

5. Conclusions

The present work provides new insight into the mechanisms governing strain delocalization in MGMCs via systematic exploration of life-like dendritic structures in MGMCs using STZ dynamics simulations. This investigation bridges the gap between atomistic and continuum methods, examining time and length scales that lie in between. Both macroscopic and microscopic characterizations are analyzed and discussed. Dendrite sizes and spacings examined spanned 7–20 nm and 17–50 nm respectively while volume fraction was held constant at ~ 64.5 %. Images of DH3 MGMC specimens were used to create the dendritic structure. Material inputs determined from a combined simulated-experimental nanoindentation approach were used in this model [99]. The following conclusions can be drawn:

- Statistical analysis of shear banding characteristics supports the hypothesis that the competition of shear band nucleation and propagation rates is the underlying mechanism encouraging strain delocalization in MGMCs. By introducing a crystalline dendritic structure into the amorphous matrix, a greater number of shear bands are encouraged to nucleate. At the same time, the crystalline dendrites also reduce the propagation or growth rates of shear bands.
- It was demonstrated that decreasing dendrite sizes yielded greater strain delocalization among more shear bands. It was also found that at these smaller microstructural sizes, the onset of run-away shear bands was delayed and overall growth rates were lower. These smaller dendrites allowed greater strain delocalization by allowing a greater fraction of the crystalline phase to participate in the shear banding process.
- These findings suggest a particular approach to utilize in the creation of less brittle MGMCs. In order to encourage more homogenous deformation, the goal is to distribute plastic strain over as many shear bands as possible. This results in a two-fold approach: 1) encourage as large a number of shear band nucleation events as possible and 2) reduce the propensity for shear bands to propagate. This can be done to a greater degree using smaller dendrites oriented randomly throughout the matrix. This allows a larger number of stress concentrations encouraging diverse shear band nucleation early on in the simulation. Smaller dendrites can also participate in shear banding which reduces their propagation rates. This in turn encourages greater shear band nucleation events to help relax the system as shear bands are not growing fast enough to do so.

Our results align with experimental findings while elucidating the underlying mechanics. They provide valuable guidance for the design of MGMCs with enhanced mechanical properties and reduced brittleness.

CRediT authorship contribution statement

Casey O. Messick: Writing – original draft, Visualization, Validation, Methodology, Investigation, Formal analysis, Data curation, Conceptualization. **Lin Li:** Writing – review & editing, Validation, Funding acquisition, Formal analysis. **Eric R. Homer:** Writing – review & editing, Validation, Supervision, Resources, Project administration, Methodology, Investigation, Funding acquisition, Formal analysis, Data curation, Conceptualization.

Declaration of competing interest

The authors declare that they have no known competing financial interests or personal relationships that could have appeared to influence the work reported in this paper.

Data availability

Data will be made available on request.

Acknowledgment

This work was supported by the National Science Foundation under Contract No. CMMI-1401777. LL was supported by the National Science Foundation under Contract No. CMMI-2331482.

Appendix A

Determination of yield strength and strain hardening rate inputs for the crystalline phase.

The Clausner expanding cavity model was developed to determine the yield stress from nanoindentation experiments [100]. The model for isotropic work hardening materials was used and the ratio of hardness (H) is given by:

$$\frac{H}{Y}=\frac{2}{3}\left[\left(1-\frac{1}{n}\right)+\left(\frac{3}{4}+\frac{1}{n}\right)\left(\frac{1}{3}\frac{E}{Y}tanY\right)^{n}\right], \tag{4}$$

where Y is the yield strength, E is the modulus, and n is the strain hardening rate. Using this model, yield strength and strain hardening rates are

systematically varied between 0.9 GPa to 1.9 GPa and 0.05 to 0.3 respectively. From prior work, a combined simulated-experimental nanoindentation approach was used to report a hardness value of 4.2 GPa for the crystalline phase [99]. Using this as the target value, a percent error map is produced (see Fig. 11). A few combinations could have been chosen that matched experimental results closely, however, a yield strength of 900 MPa and strain hardening exponent of 0.3 is chosen to match reported strain hardening rates for high entropy alloys [49,67]. High entropy alloys were chosen as the surrogate material to the crystalline phase of MGMCs because of the desire to have mechanical properties for a material with complex chemistry like that in MGMCs.

n \ Y	0.9	1.1	1.3	1.5	1.7	1.9
0.05	-31.58%					
0.1	-22.99%	-10.25%	0.58%	9.81%	17.81%	29.14%
0.2	-12.29%	-1.50%	9.93%	21.89%	33.58%	43.73%
0.3	-0.46%	12.84%	25.61%	37.04%	47.61%	57.58%

Fig. 11. Systematic variation of yield strength and strain hardening exponent.

Appendix B. Supplementary data

Supplementary data to this article can be found online at https://doi.org/10.1016/j.commatsci.2024.113253.

References

[1] W. Klement, R.H. Willens, P.O.L. Duwez, Non-crystalline Structure in Solidified Gold-Silicon Alloys, Nature 187 (4740) (1960) 869–870, https://doi.org/10.1038/187869b0.

[2] M. Telford, The case for bulk metallic glass, Mater. Today 7 (3) (2004) 36–43, https://doi.org/10.1016/S1369-7021(04)00124-5.

[3] C. Schuh, T. Hufnagel, U. Ramamurty, Mechanical behavior of amorphous alloys, Acta Mater. 55 (12) (2007) 4067–4109, https://doi.org/10.1016/j.actamat.2007.01.052.

[4] A.L. Greer, Metallic glasses on the threshold, Mater. Today 12 (1–2) (2009) 14–22, https://doi.org/10.1016/S1369-7021(09)70037-9.

[5] M.M. Trexler, N.N. Thadhani, Mechanical properties of bulk metallic glasses, Prog. Mater Sci. 55 (8) (2010) 759–839, https://doi.org/10.1016/j.pmatsci.2010.04.002.

[6] W.J. Wright, R. Saha, W.D. Nix, Deformation mechanisms of the Zr40Ti14Ni10Cu12Be24 bulk metallic glass, Mater. Trans. 42 (4) (2001) 642–649, https://doi.org/10.2320/matertrans.42.642.

[7] E.R. Homer, C.A. Schuh, Mesoscale modeling of amorphous metals by shear transformation zone dynamics, Acta Mater. 57 (9) (2009) 2823–2833, https://doi.org/10.1016/j.actamat.2009.02.035.

[8] J. Eckert, J. Das, S. Pauly, C. Duhamel, Mechanical properties of bulk metallic glasses and composites, J. Mater. Res. 22 (02) (2007) 285–301, https://doi.org/10.1557/jmr.2007.0050.

[9] D.C. Hofmann, J.-Y. Suh, A. Wiest, G. Duan, M.-L. Lind, M.D. Demetriou, W. L. Johnson, Designing metallic glass matrix composites with high toughness and tensile ductility, Nature 451 (7182) (2008) 1085–1089, https://doi.org/10.1038/nature06598.

[10] D.C. Hofmann, Bulk Metallic Glasses and Their Composites: A Brief History of Diverging Fields, J. Mater. 2013 (2013) 517904, https://doi.org/10.1155/2013/517904.

[11] C.A. Schuh, A.S. Argon, T.G. Nieh, J. Wadsworth, The transition from localized to homogeneous plasticity during nanoindentation of an amorphous metal, Phil. Mag. 83 (2003) 2585–2597, https://doi.org/10.1080/1478643031000118012.

[12] T.G. Nieh, C. Schuh, J. Wadsworth, Y. Li, Strain rate-dependent deformation in bulk metallic glasses, Intermetallics 10 (11–12) (2002) 1177–1182, https://doi.org/10.1016/S0966-9795(02)00146-2.

[13] A.V. Sergueeva, N.A. Mara, D.J. Branagan, A.K. Mukherjee, Strain rate effect on metallic glass ductility, Scr. Mater. 50 (10) (2004) 1303–1307, https://doi.org/10.1016/j.scriptamat.2004.02.019.

[14] M.B. Harris, L.S. Watts, E.R. Homer, Competition between shear band nucleation and propagation across rate-dependent flow transitions in a model metallic glass, Acta Mater. 111 (2016) 273–282, https://doi.org/10.1016/j.actamat.2016.03.066.

[15] A.V. Sergueeva, N.A. Mara, J.D. Kuntz, D.J. Branagan, A.K. Mukherjee, Shear band formation and ductility of metallic glasses, Mater. Sci. Eng. A 383 (2) (2004) 219–223, https://doi.org/10.1016/j.msea.2004.05.064.

[16] C.A. Schuh, A.C. Lund, T.G. Nieh, New regime of homogeneous flow in the deformation map of metallic glasses: elevated temperature nanoindentation experiments and mechanistic modeling, Acta Mater. 52 (20) (2004) 5879–5891, https://doi.org/10.1016/j.actamat.2004.09.005.

[17] A.S. Argon, H.Y. Kuo, Plastic flow in a disordered bubble raft (an analog of a metallic glass), Mater. Sci. Eng. 39 (1) (1979) 101–109, https://doi.org/10.1016/0025-5416(79)90174-5.

[18] E.R. Homer, Examining the initial stages of shear localization in amorphous metals, Acta Mater. 63 (2014) 44–53, https://doi.org/10.1016/j.actamat.2013.09.050.

[19] A.L. Greer, Y.Q. Cheng, E. Ma, Shear bands in metallic glasses, Mater. Sci. Eng. R. Rep. 74 (4) (2013) 71–132, https://doi.org/10.1016/j.mser.2013.04.001.

[20] T.C. Hufnagel, T. Jiao, Y. Li, L.-Q. Xing, K.T. Ramesh, Glass Under Quasi-Static and Dynamic Compression, J. Mater. Res. 17 (6) (2002) 1441–1445, https://doi.org/10.1557/JMR.2002.0214.

[21] H. Neuhäuser, Rate of shear band formation in metallic glasses, Scripta Metall 12 (1978) 471–474, https://doi.org/10.1016/0036-9748(78)90260-0.

[22] W.J. Wright, M.W. Samale, T.C. Hufnagel, M.M. LeBlanc, J.N. Florando, Studies of shear band velocity using spatially and temporally resolved measurements of strain during quasistatic compression of a bulk metallic glass, Acta Mater. 57 (16) (2009) 4639–4648, https://doi.org/10.1016/j.actamat.2009.06.013.

[23] S.X. Song, X.-L. Wang, T.G. Nieh, Capturing shear band propagation in a Zr-based metallic glass using a high-speed camera, Scr. Mater. 62 (11) (2010) 847–850, https://doi.org/10.1016/j.scriptamat.2010.02.017.

[24] T. Mukai, T.G. Nieh, Y. Kawamura, A. Inoue, K. Higashi, Effect of strain rate on compressive behavior of a Pd40Ni40P20 bulk metallic glass, Intermetallics 10 (2002) 1071–1077, https://doi.org/10.1016/S0966-9795(02)00137-1.

[25] F.H. Dalla Torre, A. Dubach, A. Nelson, J.F. Löffler, Temperature, Strain and Strain Rate Dependence of Serrated Flow in Bulk Metallic Glasses, Mater. Trans. 48 (7) (2007) 1774–1780, https://doi.org/10.2320/matertrans.MJ200782.

[26] A. Dubach, F.H. Dalla Torre, J.F. Löffler, Deformation kinetics in Zr-based bulk metallic glasses and its dependence on temperature and strain-rate sensitivity, Philos. Mag. Lett. 87 (9) (2007) 695–704, https://doi.org/10.1080/09500830701494037.

[27] A.L. Greer, I.T. Walker, Transformations in Primary Crystallites in (Fe,Ni)-Based Metallic Glasses, in: Mater. Sci. Forum, 386-388, 2002, pp. 77–88, https://doi.org/10.4028/www.scientific.net/msf.386-388.77.

[28] Y.I. Golovin, V.I. Ivolgin, V.a. Khonik, K. Kitagawa, Serrated plastic flow during nanoindentation of a bulk metallic glass, Scr. Mater. 45 (8) (2001) 947–952, https://doi.org/10.1016/S1359-6462(01)01116-2.

[29] J.H. Perepezko, S.D. Imhoff, M.-W. Chen, J.-Q. Wang, S. Gonzalez, Nucleation of shear bands in amorphous alloys, Proc. Natl. Acad. Sci. 111 (11) (2014) 3938–3942, https://doi.org/10.1073/pnas.1321518111.

[30] B. Moser, J. Kuebler, H. Meinhard, W. Muster, J. Michler, Observation of instabilities during plastic deformation by in-situ SEM indentation experiments, Adv. Eng. Mat. 7 (2005) 388–392, https://doi.org/10.1002/adem.200500049.

[31] C.A. Schuh, T.G. Nieh, Y. Kawamura, Rate Dependence of Serrated Flow During Nanoindentation of a Bulk Metallic Glass, J. Mater. Res. 17 (7) (2002) 1651–1654, https://doi.org/10.1557/JMR.2002.0243.

[32] R.D. Conner, Y. Li, W.D. Nix, W.L. Johnson, Shear band spacing under bending of Zr-based metallic glass plates, Acta Mater. 52 (8) (2004) 2429–2434, https://doi.org/10.1016/j.actamat.2004.01.034.

[33] Y. Yokoyama, Ductility improvement of Zr-Cu-Ni-Al glassy alloy, J. Non Cryst. Solids 316 (1) (2003) 104–113, https://doi.org/10.1016/S0022-3093(02)01942-7.

[34] Y. Yokoyama, K. Inoue, K. Fukaura, Cold-rolled Zr50Cu30Ni10Al10 bulk amorphous alloys with tensile plastic elongation at room temperature, Mater. Trans. 43 (12) (2002) 3199–3205, https://doi.org/10.2320/matertrans.43.3199.

[35] J. Eckert, J. Das, S. Pauly, C. Duhamel, Processing Routes, Microstructure and Mechanical Properties of Metallic Glasses and their Composites, Adv. Eng. Mater. 9 (6) (2007) 443–453, https://doi.org/10.1002/adem.200700043.

[36] R.L. Narayan, P.S. Singh, D.C. Hofmann, N. Hutchinson, K.M. Flores, U. Ramamurty, On the microstructure–tensile property correlations in bulk

metallic glass matrix composites with crystalline dendrites, Acta Mater. 60 (13–14) (2012) 5089–5100, https://doi.org/10.1016/j.actamat.2012.06.032.
[37] F. Abdeljawad, M. Fontus, M. Haataja, Ductility of bulk metallic glass composites: Microstructural effects, Appl. Phys. Lett. 98 (3) (2011) 031909, https://doi.org/10.1063/1.3531660.
[38] J. Gao, J. Sharp, D. Guan, W.M. Rainforth, I. Todd, New compositional design for creating tough metallic glass composites with excellent work hardening, Acta Mater. 86 (2015) 208–215, https://doi.org/10.1016/j.actamat.2014.11.055.
[39] W. Zhang, A.J. Bodey, T. Sui, W. Kockelmann, C. Rau, A.M. Korsunsky, J. Mi, Multi-scale Characterisation of the 3D Microstructure of a Thermally-Shocked Bulk Metallic Glass Matrix Composite, Sci. Rep. 6 (2015) 18545, https://doi.org/10.1038/srep18545.
[40] J. Qiao, H. Jia, P.K. Liaw, Metallic glass matrix composites, Mater. Sci. Eng. R. Rep. 100 (2016) 1–69, https://doi.org/10.1016/j.mser.2015.12.001.
[41] M.L. Lee, Y. Li, C.A. Schuh, Effect of a controlled volume fraction of dendritic phases on tensile and compressive ductility in La-based metallic glass matrix composites, Acta Mater. 52 (14) (2004) 4121–4131, https://doi.org/10.1016/j.actamat.2004.05.025.
[42] Y. Zhang, W. Xu, H. Tan, Y. Li, Microstructure control and ductility improvement of La-Al-(Cu, Ni) composites by Bridgman solidification, Acta Mater. 53 (9) (2005) 2607–2616, https://doi.org/10.1016/j.actamat.2005.02.020.
[43] S. Pauly, J. Das, J. Bednarcik, N. Mattern, K.B. Kim, D.H. Kim, J. Eckert, Deformation-induced martensitic transformation in Cu-Zr-(Al, Ti) bulk metallic glass composites, Scr. Mater. 60 (6) (2009) 431–434, https://doi.org/10.1016/j.scriptamat.2008.11.015.
[44] D.C. Hofmann, J.-Y. Suh, A. Wiest, M.-L. Lind, M.D. Demetriou, W.L. Johnson, Development of tough, low-density titanium-based bulk metallic glass matrix composites with tensile ductility, Proc. Natl. Acad. Sci. 105 (51) (2008) 20136–20140, https://doi.org/10.1073/pnas.0809000106.
[45] X.L. Fu, Y. Li, C.A. Schuh, Temperature, strain rate and reinforcement volume fraction dependence of plastic deformation in metallic glass matrix composites, Acta Mater. 55 (9) (2007) 3059–3071, https://doi.org/10.1016/j.actamat.2007.01.009.
[46] J.C. Lee, Y.C. Kim, J.P. Ahn, H.S. Kim, Enhanced plasticity in a bulk amorphous matrix composite: Macroscopic and microscopic viewpoint studies, Acta Mater. 53 (1) (2005) 129–139, https://doi.org/10.1016/j.actamat.2004.09.010.
[47] J.W. Qiao, J.T. Zhang, F. Jiang, Y. Zhang, P.K. Liaw, Y. Ren, G.L. Chen, Development of plastic Ti-based bulk-metallic-glass-matrix composites by controlling the microstructures, Mater. Sci. Eng. A 527 (29–30) (2010) 7752–7756, https://doi.org/10.1016/j.msea.2010.08.055.
[48] M.E. Launey, D.C. Hofmann, J.Y. Suh, H. Kozachkov, W.L. Johnson, R.O. Ritchie, Fracture toughness and crack-resistance curve behavior in metallic glass-matrix composites, Appl. Phys. Lett. 94 (2009) 2009–2011, https://doi.org/10.1063/1.3156026.
[49] D.C. Hofmann, J.Y. Suh, A. Wiest, G. Duan, M.-L. Lind, M.D. Demetriou, W. L. Johnson, Designing Bulk Metallic Glass Matrix Composites with High Toughness and Tensile Ductility, Nature 451 (2008) 1085–1089, https://doi.org/10.1038/nature06598.
[50] J.L. Cheng, G. Chen, F. Xu, Y.L. Du, Y.S. Li, C.T. Liu, Correlation of the microstructure and mechanical properties of Zr-based in-situ bulk metallic glass matrix composites, Intermetallics 18 (12) (2010) 2425–2430, https://doi.org/10.1016/j.intermet.2010.08.040.
[51] T. Zhang, H.Y. Ye, J.Y. Shi, H.J. Yang, J.W. Qiao, Dendrite size dependence of tensile plasticity of in situ Ti-based metallic glass matrix composites, J. Alloy. Compd. 583 (2014) 593–597, https://doi.org/10.1016/j.jallcom.2013.08.201.
[52] C.C. Hays, C.P. Kim, W.L. Johnson, Microstructure controlled shear band pattern formation and enhanced plasticity of bulk metallic glasses containing in situ formed ductile phase dendrite dispersions, Phys. Rev. Lett. 84 (13) (2000) 2901–2904, https://doi.org/10.1103/PhysRevLett.84.2901.
[53] S.H. Hong, J.T. Kim, M.W. Lee, J.M. Park, M.H. Lee, B.S. Kim, J.Y. Park, Y. Seo, J. Y. Suh, P. Yu, M. Qian, K.B. Kim, Combinatorial influence of bimodal size of B2 TiCu compounds on plasticity of Ti-Cu-Ni-Zr-Sn-Si bulk metallic glass composites, Metall. Mater. Trans. A 45 (5) (2014) 2376–2381, https://doi.org/10.1007/s11661-013-1947-9.
[54] L. Zhang, T. Yan, D. Şopu, Y. Wu, B. Jiang, K. Du, H. Zhang, J. Eckert, Shear-band blunting governs superior mechanical properties of shape memory metallic glass composites, Acta Mater 241 (2022) 118422, https://doi.org/10.1016/j.actamat.2022.118422.
[55] C.C. Hays, W.L. Johnson, C.N.P. Kim, Enhanced Plasticity of Bulk Metallic Glasses Containing Ductile Phase Dendrite Dispersions, Mat. Sci. Forum 343 (2000) 191–196, https://doi.org/10.4028/www.scientific.net/MSF.343-346.191.
[56] C.E. Packard, E.R. Homer, N. Al-Aqeeli, C.A. Schuh, Cyclic hardening of metallic glasses under Hertzian contacts: Experiments and STZ dynamics simulations, Phil. Mag. 90 (10) (2010) 1373–1390, https://doi.org/10.1080/14786430903352664.
[57] T.J. Hardin, E.R. Homer, Microstructural factors of strain delocalization in model metallic glass matrix composites, Acta Mater. 83 (2015) 203–215, https://doi.org/10.1016/j.actamat.2014.09.043.
[58] K. Durst, M. Göken, H. Vehoff, Finite element study for nanoindentation measurements on two-phase materials, J. Mater. Res. 19 (2004) 85–93, https://doi.org/10.1557/jmr.2004.19.1.85.
[59] A.A. Pelegri, X. Huang, Nanoindentation on soft film/hard substrate and hard film/soft substrate material systems with finite element analysis, Compos. Sci. Technol. 68 (1) (2008) 147–155, https://doi.org/10.1016/j.compscitech.2007.05.033.
[60] Z.H. Xu, D. Rowcliffe, Finite element analysis of substrate effects on indentation behaviour of thin films, Thin Solid Films 447–448 (03) (2004) 399–405, https://doi.org/10.1016/S0040-6090(03)01071-X.
[61] X. Huang, A.A. Pelegri, Finite element analysis on nanoindentation with friction contact at the film/substrate interface, Compos. Sci. Technol. 67 (7–8) (2007) 1311–1319, https://doi.org/10.1016/j.compscitech.2006.10.005.
[62] G.M. Pharr, A. Bolshakov, T.Y. Tsui, J.C. Hay, Nanoindentation of soft films on hard substrates: experiments and finite element simulations, MRS Online Proceedings Library 505 (1997) 109–120, https://doi.org/10.1557/PROC-505-109.
[63] J.W. Qiao, A.C. Sun, E.W. Huang, Y. Zhang, P.K. Liaw, C.P. Chuang, Tensile deformation micromechanisms for bulk metallic glass matrix composites: From work-hardening to softening, Acta Mater. 59 (10) (2011) 4126–4137, https://doi.org/10.1016/j.actamat.2011.03.036.
[64] E.R. Homer, Modeling the Mechanical Behavior of Amorphous Metals by Shear Transformation Zone Dynamics, MIT Ph.D. Thesis (2010) http://hdl.handle.net/1721.1/59005.
[65] O.N. Senkov, G.B. Wilks, J.M. Scott, D.B. Miracle, Mechanical properties of Nb25Mo25Ta25W25 and V20Nb20Mo20Ta20W20 refractory high entropy alloys, Intermetallics 19 (5) (2011) 698–706, https://doi.org/10.1016/j.intermet.2011.01.004.
[66] Y. Zhang, T.T. Zuo, Z. Tang, M.C. Gao, K.A. Dahmen, P.K. Liaw, Z.P. Lu, Microstructures and properties of high-entropy alloys, Prog Mater Sci 61 (2014) 1–93, https://doi.org/10.1016/j.pmatsci.2013.10.001.
[67] A.J. Zaddach, R.O. Scattergood, C.C. Koch, Tensile properties of low-stacking fault energy high-entropy alloys, Mater. Sci. Eng. A 636 (2015) 373–378, https://doi.org/10.1016/j.msea.2015.03.109.
[68] B. Gludovatz, E.P. George, R.O. Ritchie, Processing, Microstructure and Mechanical Properties of the CrMnFeCoNi High-Entropy Alloy, JOM 67 (10) (2015) 2262–2270, https://doi.org/10.1007/s11837-015-1589-z.
[69] G. Dirras, H. Couque, L. Lilensten, A. Heczel, D. Tingaud, J.-P. Couzinié, L. Perrière, J. Gubicza, I. Guillot, Mechanical behavior and microstructure of Ti20Hf20Zr20Ta20Nb20 high-entropy alloy loaded under quasi-static and dynamic compression conditions, Mater Charact 111 (2016) 106–113, https://doi.org/10.1016/j.matchar.2015.11.018.
[70] H. Zhou, S. Qu, W. Yang, An atomistic investigation of structural evolution in metallic glass matrix composites, Int. J. Plast 44 (2013) 147–160, https://doi.org/10.1016/j.ijplas.2013.01.002.
[71] J. Das, M.B. Tang, K.B. Kim, R. Theissmann, F. Baier, W.H. Wang, J. Eckert, Work-Hardenable' Ductile Bulk Metallic Glass, Phys. Rev. Lett. 94 (20) (2005) 205501, https://doi.org/10.1103/PhysRevLett.94.205501.
[72] K. Hajlaoui, A.R. Yavari, B. Doisneau, A. LeMoulec, G. Vaughan, A.L. Greer, A. Inoue, W. Zhang, Å. Kvick, Shear delocalization and crack blunting of a metallic glass containing nanoparticles: In situ deformation in TEM analysis, Scr. Mater. 54 (11) (2006) 1829–1834, https://doi.org/10.1016/j.scriptamat.2006.02.030.
[73] J. Eckert, J. Das, G. He, M. Calin, K.B. Kim, Ti-base bulk nanostructure-dendrite composites: Microstructure and deformation, Mater. Sci. Eng. A 449–451 (2007) 24–29, https://doi.org/10.1016/j.msea.2006.02.236.
[74] H. Choi-Yim, W.L. Johnson, Bulk metallic glass matrix composites, Appl. Phys. Lett. 71 (26) (1997) 3808–3810, https://doi.org/10.1063/1.120512.
[75] J.H. Chen, M.Q. Jiang, Y. Chen, L.H. Dai, Strain rate dependent shear banding behavior of a Zr-based bulk metallic glass composite, Mater. Sci. Eng. A 576 (2013) 134–139, https://doi.org/10.1016/j.msea.2013.03.082.
[76] J.W. Qiao, H.Y. Ye, Y.S. Wang, S. Pauly, H.J. Yang, Z.H. Wang, Distinguished work-hardening capacity of a Ti-based metallic glass matrix composite upon dynamic loading, Mater. Sci. Eng. A 585 (2013) 277–280, https://doi.org/10.1016/j.msea.2013.07.027.
[77] Y.S. Wang, G.J. Hao, J.W. Qiao, Y. Zhang, J.P. Lin, High strain rate compressive behavior of Ti-based metallic glass matrix composites, Intermetallics 52 (2014) 138–143, https://doi.org/10.1016/j.intermet.2014.03.012.
[78] J.P. Schramm, D.C. Hofmann, M.D. Demetriou, W.L. Johnson, Metallic-glass-matrix composite structures with benchmark mechanical performance, Appl. Phys. Lett. 97 (24) (2010) 241910, https://doi.org/10.1063/1.3521412.
[79] F. Szuecs, C.P. Kim, W.L. Johnson, Mechanical properties of Zr56.2Ti13.8Nb5.0Cu6.9Ni5.6Be12.5 ductile phase reinforced bulk metallic glass composite, Acta Mater. 49 (9) (2001) 1507–1513, https://doi.org/10.1016/S1359-6454(01)00068-4.
[80] J.W. Qiao, S. Wang, Y. Zhang, P.K. Liaw, G.L. Chen, Large plasticity and tensile necking of Zr-based bulk-metallic-glass-matrix composites synthesized by the Bridgman solidification, Appl. Phys. Lett. 94 (15) (2009) 2007–2010, https://doi.org/10.1063/1.3118587.
[81] M. Martin, L. Kecskes, N.N. Thadhani, High-strain-rate dynamic mechanical behavior of a bulk metallic glass composite, J. Mater. Res. 23 (4) (2008) 998–1008, https://doi.org/10.1557/jmr.2008.0119.
[82] C. Fan, R.T. Ott, T.C. Hufnagel, Metallic glass matrix composite with precipitated ductile reinforcement, Appl. Phys. Lett. 81 (6) (2002) 1020–1022, https://doi.org/10.1063/1.1498864.
[83] R.T. Ott, C. Fan, J. Li, T.C. Hufnagel, Structure and properties of Zr-Ta-Cu-Ni-Al bulk metallic glasses and metallic glass matrix composites, J. Non Cryst. Solids (2003) 158–163, https://doi.org/10.1016/S0022-3093(02)01996-8.
[84] S. Guo, C. Su, Micro/nano ductile-phases reinforced Fe-based bulk metallic glass matrix composite with large plasticity, Mater. Sci. Eng. A 707 (2017) 44–50, https://doi.org/10.1016/j.msea.2017.09.036.
[85] J.M. Park, S.W. Sohn, T.E. Kim, D.H. Kim, K.B. Kim, W.T. Kim, Nanostructure-dendrite composites in the Fe-Zr binary alloy system exhibiting high strength and

plasticity, Scr. Mater. 57 (12) (2007) 1153–1156, https://doi.org/10.1016/j.scriptamat.2007.08.004.
[86] J.M. Gentile, D.C. Hofmann, J.R. Trelewicz, Microstructural dependence of the incipient to homogeneous flow transition in metallic glass composites, Scr. Mater. 188 (2020) 32–36, https://doi.org/10.1016/j.scriptamat.2020.06.066.
[87] J.M. Gentile, D.D. Stauffer, D.C. Hofmann, J.R. Trelewicz, Shear localization and its dependence on microstructural length scales in metallic glass composites, Materialia 9 (2020) 100598, https://doi.org/10.1016/j.mtla.2020.100598.
[88] D. Kammer, P.W. Voorhees, The morphological evolution of dendritic microstructures during coarsening, Acta Mater. 54 (6) (2006) 1549–1558, https://doi.org/10.1016/j.actamat.2005.11.031.
[89] Q.K. Li, M. Li, Assessing the critical sizes for shear band formation in metallic glasses from molecular dynamics simulation, Appl. Phys. Lett. 91 (23) (2007) 231905, https://doi.org/10.1063/1.2821832.
[90] E.R. Homer, D. Rodney, C.A. Schuh, Kinetic Monte Carlo study of activated states and correlated shear-transformation-zone activity during the deformation of an amorphous metal, Phys. Rev. B 81 (2010) 064204, https://doi.org/10.1103/PhysRevB.81.064204.
[91] C.E. Packard, C.A. Schuh, Initiation of shear bands near a stress concentration in metallic glass, Acta Mater. 55 (16) (2007) 5348–5358, https://doi.org/10.1016/j.actamat.2007.05.054.
[92] R.L. Narayan, P.S. Singh, D.C. Hofmann, N. Hutchinson, K.M. Flores, U. Ramamurty, On the microstructure-tensile property correlations in bulk metallic glass matrix composites with crystalline dendrites, Acta Mater. 60 (13–14) (2012) 5089–5100, https://doi.org/10.1016/j.actamat.2012.06.032.
[93] Y.S. Wang, G.J. Hao, Y. Zhang, J.P. Lin, L. Song, J.W. Qiao, The role of the interface in a Ti-based metallic glass matrix composite with in situ dendrite reinforcement, Surf. Interface Anal. 46 (5) (2014) 293–296, https://doi.org/10.1002/sia.5413.
[94] G. Wu, K.C. Chan, L. Zhu, L. Sun, J. Lu, Dual-phase nanostructuring as a route to high-strength magnesium alloys, Nature 545 (7652) (2017) 80–83, https://doi.org/10.1038/nature21691.
[95] G. Wu, C. Liu, L. Sun, Q. Wang, B. Sun, B. Han, J.-J. Kai, J. Luan, C.T. Liu, K. Cao, Y. Lu, L. Cheng, J. Lu, Hierarchical nanostructured aluminum alloy with ultrahigh strength and large plasticity, Nat. Commun. 10 (1) (2019) 5099, https://doi.org/10.1038/s41467-019-13087-4.
[96] Y. Wang, J. Li, A.V. Hamza, T.W. Barbee, Ductile crystalline-amorphous nanolaminates, PNAS 104 (27) (2007) 11155–11160, https://doi.org/10.1073/pnas.0702344104.
[97] Y. Gu, J. Cappola, J. Wang, L. Li, A Hall-Petch-like relationship linking nanoscale heterogeneity to yield stress of heterogeneous metallic glasses, Int. J. Plast 170 (2023) 103759, https://doi.org/10.1016/j.ijplas.2023.103759.
[98] J. Cappola, J. Wang, L. Li, A dislocation-density-based crystal plasticity model for FCC nanocrystalline metals incorporating thermally-activated depinning from grain boundaries, Int. J. Plast 172 (2024) 103863, https://doi.org/10.1016/j.ijplas.2023.103863.
[99] C.O. Messick, Examining the Mechanics Responsible for Strain Delocalization in Metallic Glass Matrix Composites, BYU M.S. Thesis, (2018) https://scholarsarchive.byu.edu/etd/7043.
[100] A. Clausner, F. Richter, Determination of yield stress from nano-indentation experiments, Eur. J. Mech. A. Solids 51 (2015) 11–20, https://doi.org/10.1016/j.euromechsol.2014.11.008.